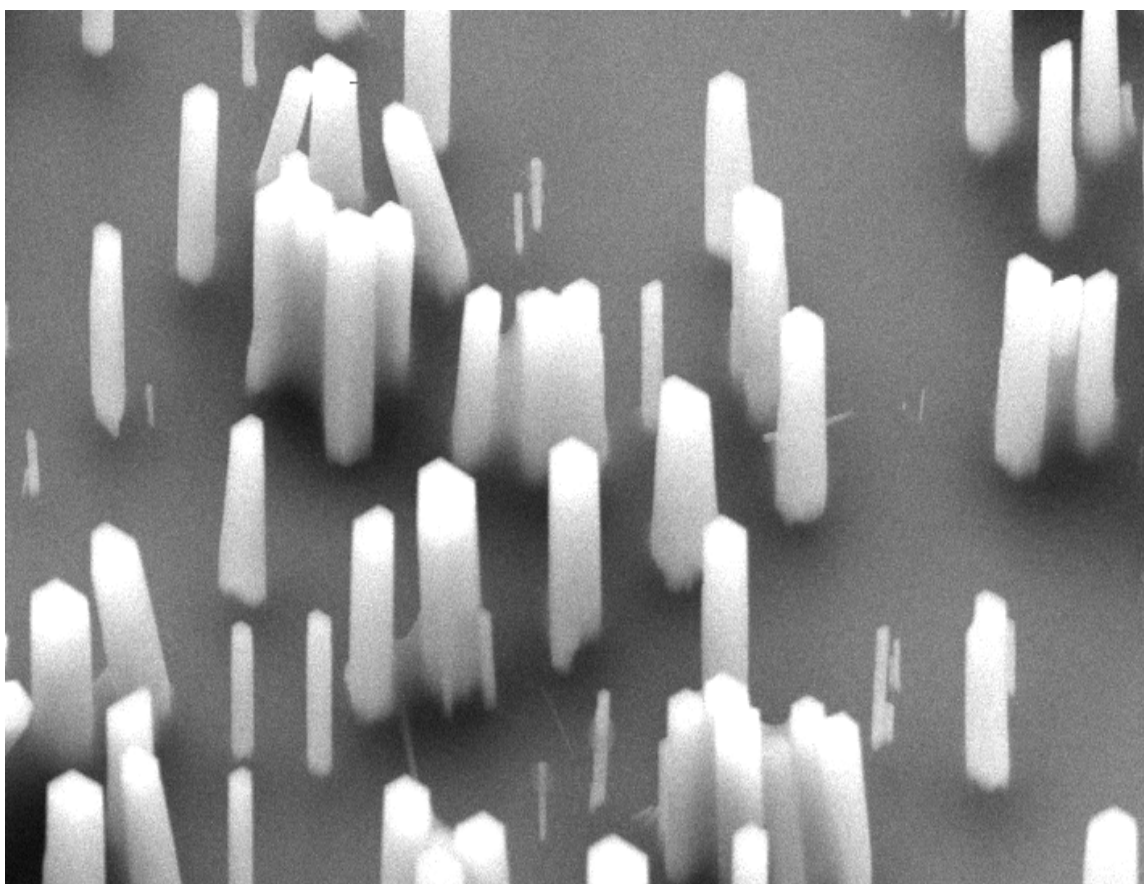


Chapter 5

Correlated Unidirectional Behavior in Zinc Oxide Nanowires[†]



[†]adapted from D.-S. Yang, C. Lao, A. H. Zewail, *Science* **321**, 1660 (2008).

Introduction

Major changes in the physical, chemical or optical properties of a substance can occur as a result of shrinking dimension and changing morphology down to the nanometer scale, primarily because of quantum confinement and surface effects. Quantum dots and nanotubes are examples of such structures, which have the potential for a variety of applications (for reviews, see Refs. 1–7). Among the materials that show promising features for optoelectronics, such as blue-green laser diodes and photonic devices, the wide-gap semiconductor zinc oxide (ZnO) has been one of the most investigated nanowire materials (8, 9). At the nanoscale, design of such structures requires fundamental understanding of electronic and nuclear degrees of freedom in the unique nanowire architecture, because they control the effective carrier mobility and properties along the wires. With optical methods (for a review, see Ref. 10), the transient response can be probed, but, because of the wavelengths involved, the atomic-scale structural changes are not determined; electrons of the appropriate wavelength provide the means for the visualization of both.

In this chapter, I present the visualization of the structure and dynamics of vertically aligned ZnO nanowires using ultrafast electron crystallography (UEC). Their unique pancake-type diffraction is the result of the ordered structure together with electron refraction due to the shape of the hexagonal rod-like nanowires. Following electronic excitation of this wide-gap photonic material, the wires were found to exhibit colossal expansions, two orders of magnitude higher than that expected at thermal equilibrium. The expansion is highly anisotropic, a quasi-one-dimensional behavior, and is facilitated by the induced antibonding character. By reducing the density of nanowires, the expansions reach even larger values and occur at shorter times, suggesting a decrease of

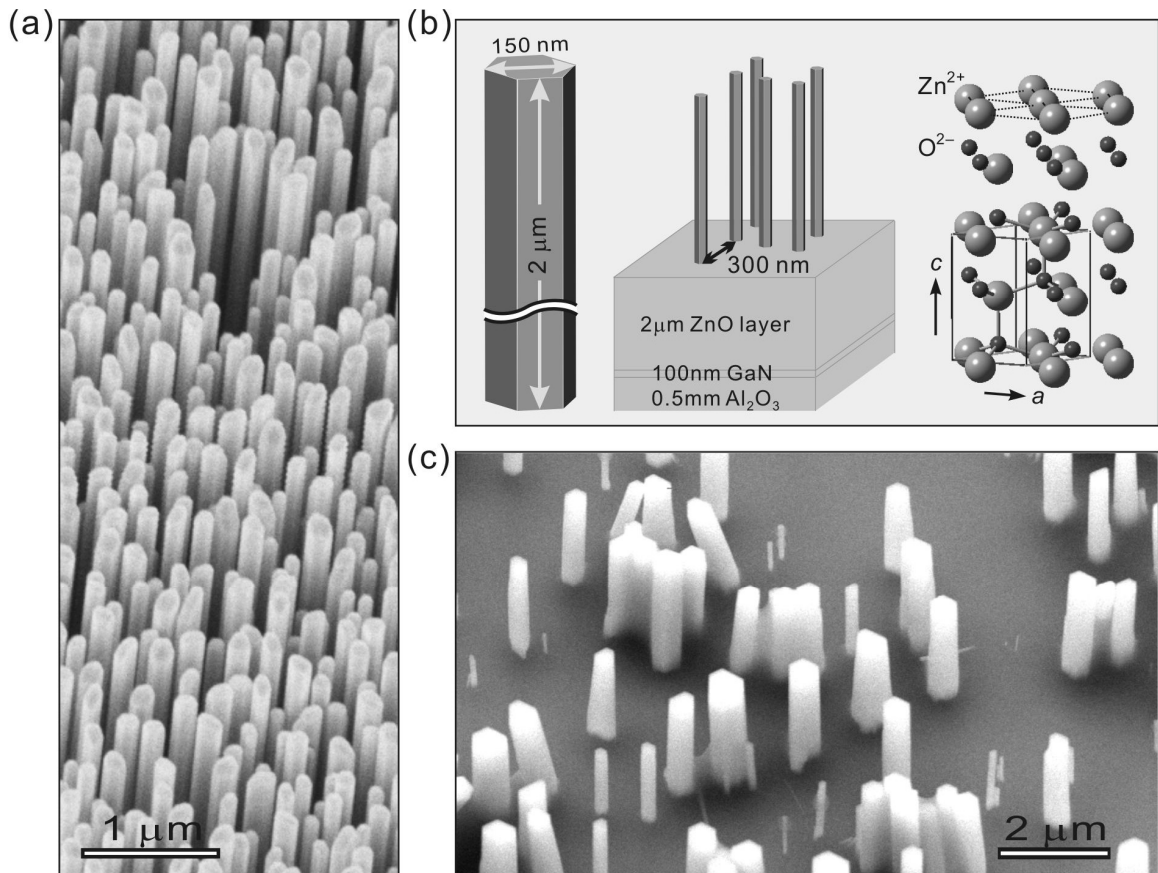


Fig. 1. Scanning electron micrographs and structure of ZnO nanowires. (a) The SEM image of the array fabricated through physical vapor deposition. The high-density wires are vertically aligned. Gold nanoparticles may be present dispersively as a result of the catalyst-assisted synthesis (11). (b) The structure (from the known inorganic crystal structure database) together with a schematic showing the average diameter and length of a single wire, the average spacing between wires, and the layer composition below the ZnO array sample. (c) The SEM image of the array fabricated through hydrothermal synthesis. The vertically aligned wires are thicker, on the average, and form an array with a much lower density. No gold nanoparticles are present in the nanowires, since a metallic catalyst is not required for this wet-chemistry synthesis method (12).

the structural constraint in transient atomic motions. This unanticipated ultrafast carrier-driven expansion highlights the optoelectronic consequences of nanometer-scale morphologies.

Materials and Experimental Section

The nanowire array was synthesized via a bottom-up process of physical vapor deposition (11). A single-crystal sapphire of $(11\bar{2}0)$ surface with a 100-nm GaN layer (grown by metal-organic chemical vapor deposition) was used as the collection substrate. Reaction parameters such as the chamber pressure, temperature and the gas flow rate were varied to obtain the nanowires, which were supported by a $\sim 2\text{-}\mu\text{m}$ layer of ZnO on the substrate, were obtained as a vertically aligned array. As shown in Fig. 1, panels a and b, the wires have an average diameter of $\sim 150\text{ nm}$, a length of $\sim 2\text{ }\mu\text{m}$, and an average spacing of $\sim 300\text{ nm}$. We also studied nanowires prepared by an entirely different method [hydrothermal synthesis (12)], and for this case the density of wires is notably lower, as seen in Fig. 1c. Both specimens were characterized by scanning electron microscopy (SEM) (Fig. 1, panels a and c); transmission electron microscopy and X-ray diffraction measurements have also been used to characterize the products of the two aforementioned methods (11, 12).

Electron packets at near grazing angles ($\theta_{\text{in}} = 2.7^\circ$) were invoked in our UEC apparatus. A heating pulse preceded in time the electron packet and was used to excite the carriers of the wires. Frames of the far-field diffraction were recorded at different delay times and with the scheme of pulse tilting (for velocity mismatch compensation), which enabled the reported spatiotemporal resolution (13-16). Within the experimental repetition period of 1 ms, the sample at room temperature fully recovers to the initial

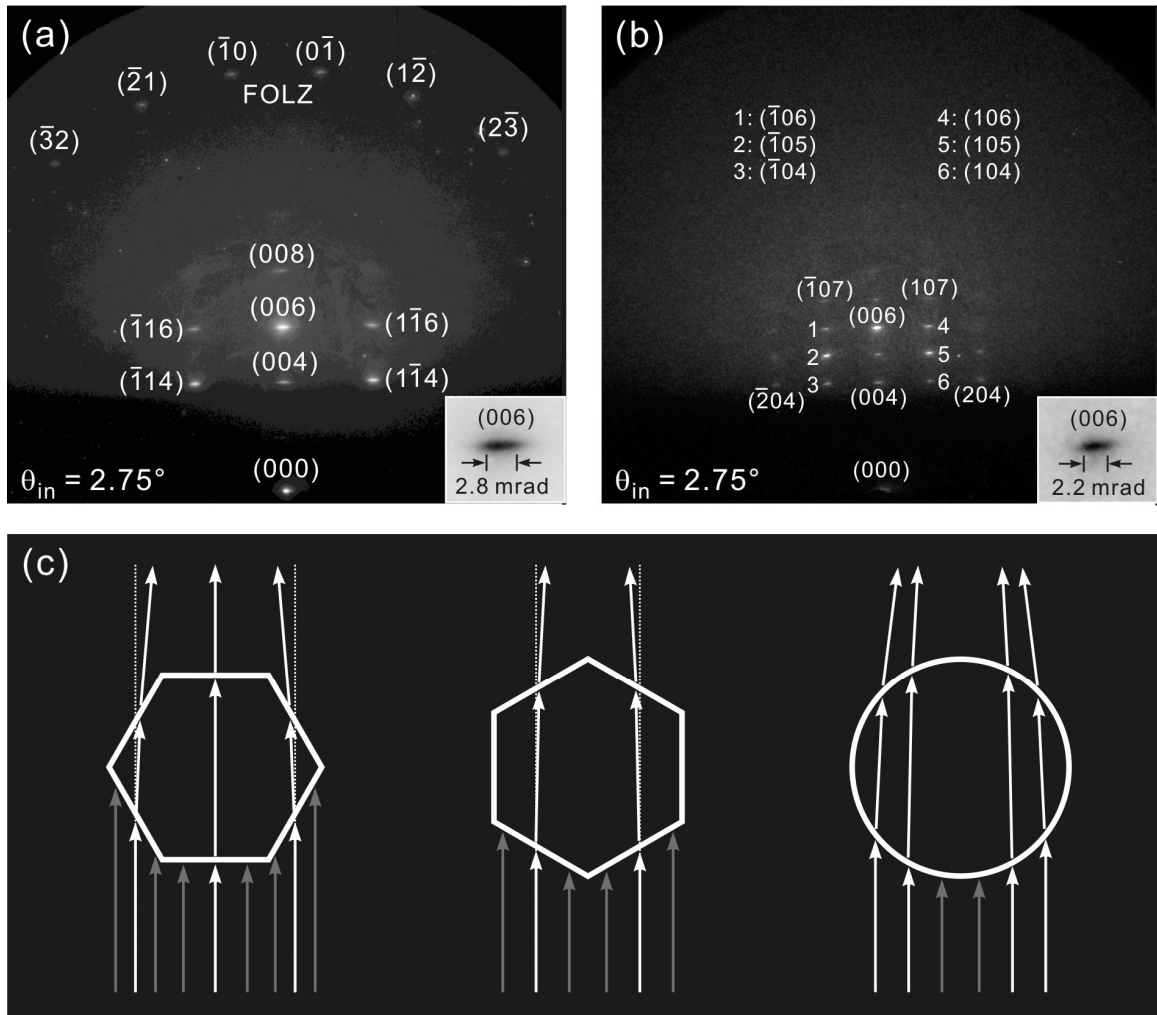


Fig. 2. Pancake-type diffraction and the shape effect of nanowires. The diffraction patterns were obtained at an incidence angle of $\theta_{in} = 2.75^\circ$, with the electron beam propagating along the [110] direction (a) and the [100] direction (b). From the well-indexed Bragg spots and FOLZ diffractions, the wurtzite ZnO structure is determined; the undiffracted (unblocked) electrons form the (000) spot. The insets show the enlarged horizontal width of the (006) Bragg spot. (c) Refraction of the probing electrons at the vacuum/material interface, and the overall beam deflection caused by the different orientations and geometries of a nanowire (top view).

ground state. This recovery was confirmed by observing no change in the diffraction patterns whether recorded at negative delay time (an effective 1-ms delay) or without the excitation. From the observed intensities, positions, and widths of the Bragg diffractions, we obtained the change of atomic positions with time, the structural factor, and the transient inhomogeneity in the wires. The initial rise of signals was checked by using time delays of 2 ps. The polarization was parallel to the cross section of wires, and in order to ensure uniform excitation of the target region, the electron-probed area on the sample was kept relatively small (~1 mm versus 3 mm for the full-width of the heating-pulse footprint at half maximum). By varying the fluence, the influence of carrier density on structural dynamics was examined, and in this case the wires were directly excited. The maximum optical fluence applied was 22.5 mJ/cm². Finally, by using two arrays of nanowires, the effect of their packing density on the substrate was elucidated.

Nanowire Structure and Electron Diffraction

The static structure of the ZnO nanowires without the optical excitation was determined by recording the diffraction patterns at different incidence angles (rocking curves); patterns of two zone axes are given in Fig. 2, panels a and b. With the electron beam propagating along the [110] direction, the patterns consist of both the Bragg spots and the first-order-Laue-zone (FOLZ) diffractions (17), and all have horizontally elongated (“pancake”) shapes, as seen in Fig. 2a. With a 30° rotation of the specimen, the electron beam becomes directed along the [100] axis, and we only observe the Bragg spots at a larger incidence angle; this is because the FOLZ diffractions are out of the camera region (Fig. 2b). The spacings between the diffraction spots (from the center of the pancakes) translate to the lattice constants of $a = b = 3.25(0)$ Å and $c = 5.20(8)$ Å,

entirely consistent with the values for a wurtzite structure of ZnO crystals obtained by x-ray diffraction and calculations (10, 18).

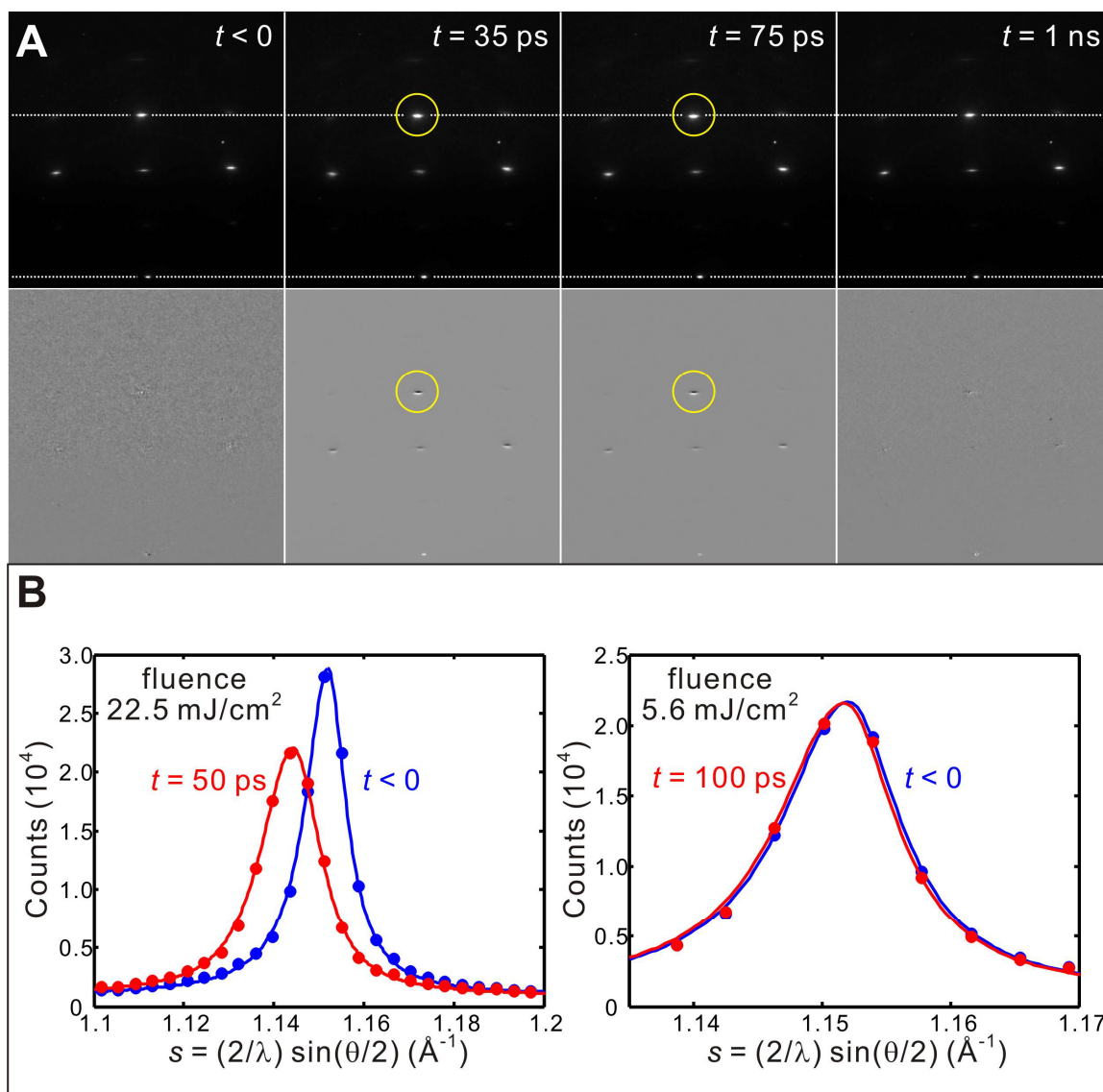
The pancake horizontal shape of the Bragg spots (Fig. 2, insets of panels a and b) is distinct from the spots seen in bulk crystal diffraction and mirrors the hexagonal nanostructured wire. Because of the wires' nanometer-scale geometry and the attractive inner potential (V_1) inside the material, the diffracted electron beam is refracted and gives rise to a horizontal spread. Quantitatively, this geometry effect can be described by considering the analogue of Snell's law in optics (19), giving:

$$\sin \theta_{\text{vac}} = (1 + eV_1/E_k)^{1/2} \sin \theta_1, \quad (1)$$

where θ_{vac} and θ_1 are, respectively, the angles in the vacuum and inside the wires, with respect to the surface normal, and E_k is the kinetic energy of the incident electron, which is 30 keV in our case (see also Sec. A.4.3 of Ch. 2). In general, when the surface layers are parallel and $eV_1 \ll E_k$, as in typical UEC experiments (see, e.g., Chs. 4, 6 and 7), this effect is negligible, but for the nanowires the situation is different (see Fig. 2c), and the refraction can be invoked to obtain the geometry of the wires.

Here, we should emphasize that the direct electron beam has a horizontal FWHM of ~ 1.8 mrad on the camera screen, which is smaller than the observed spreads of 2.8 and 2.2 mrad for the two orientations. Given the relatively large diameter of the nanowires (~ 150 nm), the Scherrer-type broadening [$D \cdot \Delta s \sim 1$ where D is the particle size and Δs is the scattering spread on the screen (20); see also Eq. 23 of Ch. 2] is only < 0.05 mrad. Most importantly, the vertical width of Bragg spots is much narrower than the horizontal one for the same electron beam used (Fig. 2).

For a hexagonal wire, with the two orientations of 30° rotation difference (Fig. 2c,



(See next page for the figure caption.)

Fig. 3 (a) Diffraction images (upper panel) and differences (lower panel) at selective delay times. In the original images, the movement of the (006) spot can be seen (yellow circles); the upper dashed line indicates its initial vertical position before excitation. Stationary nature of the (000) direct beam (referenced by the lower dashed line) is evident. The diffraction spots move downward at early times, as indicated by intensity losses (black) at the original positions and gains (white) at lower positions; at longer time the disappearance of diffraction difference signifies the recovery of the excited ZnO nanowires. (b) Vertical cross section of diffraction profiles for the (006) Bragg spot and the fits to pseudo-Voigt functions, at two selective delay times (blue and red), and at the highest (left panel) and lowest (right panel) fluences used. Here, s is the scattering vector and θ is the total deflection angle from the direct beam to the diffraction spot. Temporal evolution of the peak position, intensity and width was obtained from the fits at different delay times. The small shift of the diffraction peak at the lowest fluence well demonstrates the sensitivity of the UEC detection (see Fig. 4b).

left and middle panels), there are two angles of deflection, $\sqrt{3}V_1/E_k$ and $V_1/\sqrt{3}E_k$, respectively. Thus, the intensity profile of the pancake is the sum of the contributions from the center and the two sides of the hexagon. For a cylindrical wire (Fig. 2c, right), the intensity profile is determined by the deflections, $\tan\theta_{\text{vac}}(V_1/E_k)$, with a width which resembles the case shown on the left of Fig. 2c. The difference between the two geometries is easy to discern: if circular, the rotation of the nanostructure would give no variation in the horizontal spot width, which is inconsistent with the experimental observation. For ZnO, the inner potential V_1 is 15.9 V (21). With the camera being 16.8 cm away from the nanowires, additional diffraction intensities near ± 0.92 mrad (Fig. 2c, left) and ± 0.31 mrad (Fig 2c, middle) result in the horizontal spread from the spot center. Accordingly, this shape effect properly accounts for the observations made for the two zone axes (Fig. 2, panels a and b). Moreover, from the fact that the probing direction in Fig. 2a is [110] we determine the facets of nanowires to be of {110}, which is again consistent with the preferential growth (11). It should be noted that the vertical spot width did not increase, a consequence of the unique elongated geometry.

Laser-induced Dynamics of ZnO Nanowires

Structural dynamics of the wires were obtained from the diffraction frames at different delay times, following the optical excitation. The intensity decrease and vertical spot movement for each Bragg spot were evident in the diffraction. While all of the diffraction spots move downward at early times and recover the original positions at longer times, the unblocked (undiffracted) direct beam did not change, thus eliminating the possibility of surface charging or surface potential change at all fluences used (Fig. 3a; in a later section, we shall address an issue raised with regard to the extent of movement

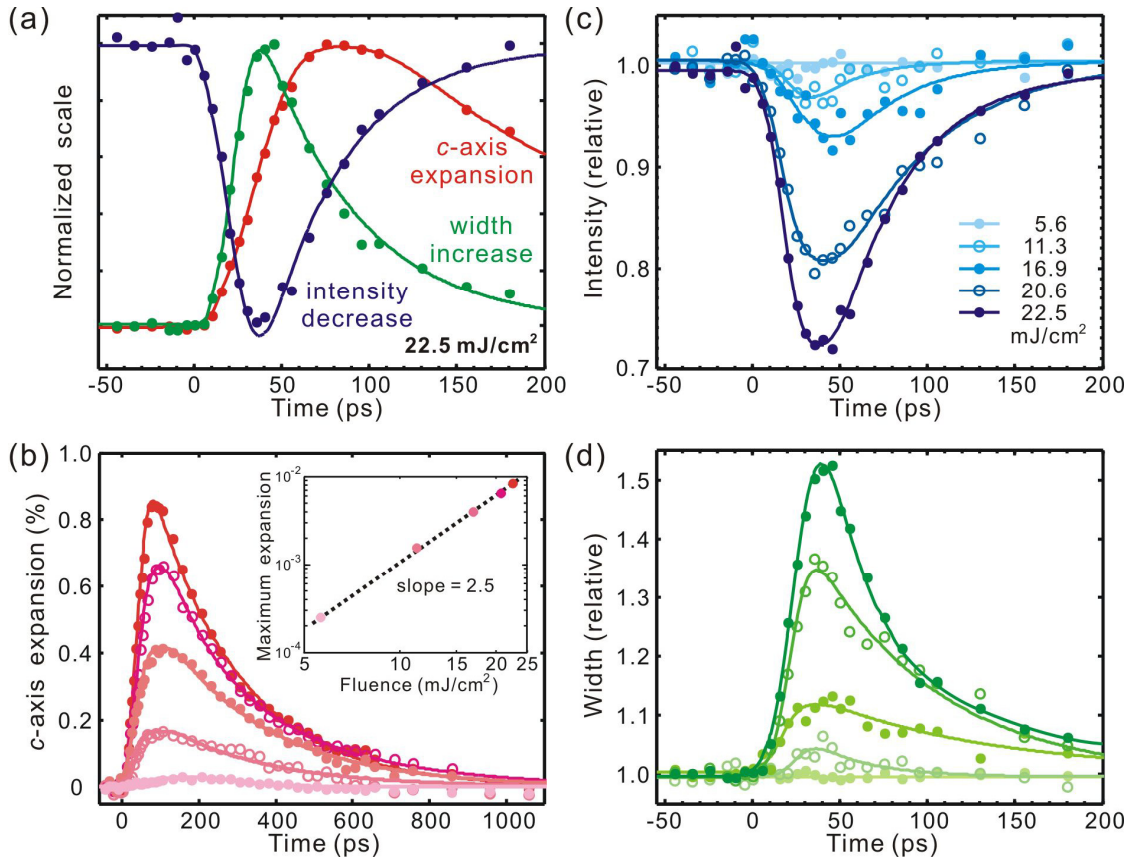


Fig. 4. Structural dynamics. Changes of the c -axis expansion, diffraction intensity and width of the (006) Bragg spot with time and at different excitation fluences. All solid lines are fits to the data. (a) The intensity decrease (blue dots) and width increase (green dots) behave similarly, and precede the buildup of structural expansion (red dots). In ~ 200 ps the former two diffraction features almost recover the original values, whereas the decay of expansion appears on a longer (nanosecond) time scale. (b) A significantly larger c -axis expansion was obtained at higher excitation fluences. The fitted slope in the log–log plot (inset) indicates that the maximum expansion is proportional to the fluence to the power of 2.5. At all fluences, however, the expanded nanowires nearly return to their original structure in ~ 1 ns. (c and d) A more significant intensity decrease and a larger width increase are observed following a stronger excitation. At the lowest fluence used, however, no appreciable diffraction changes are observed.

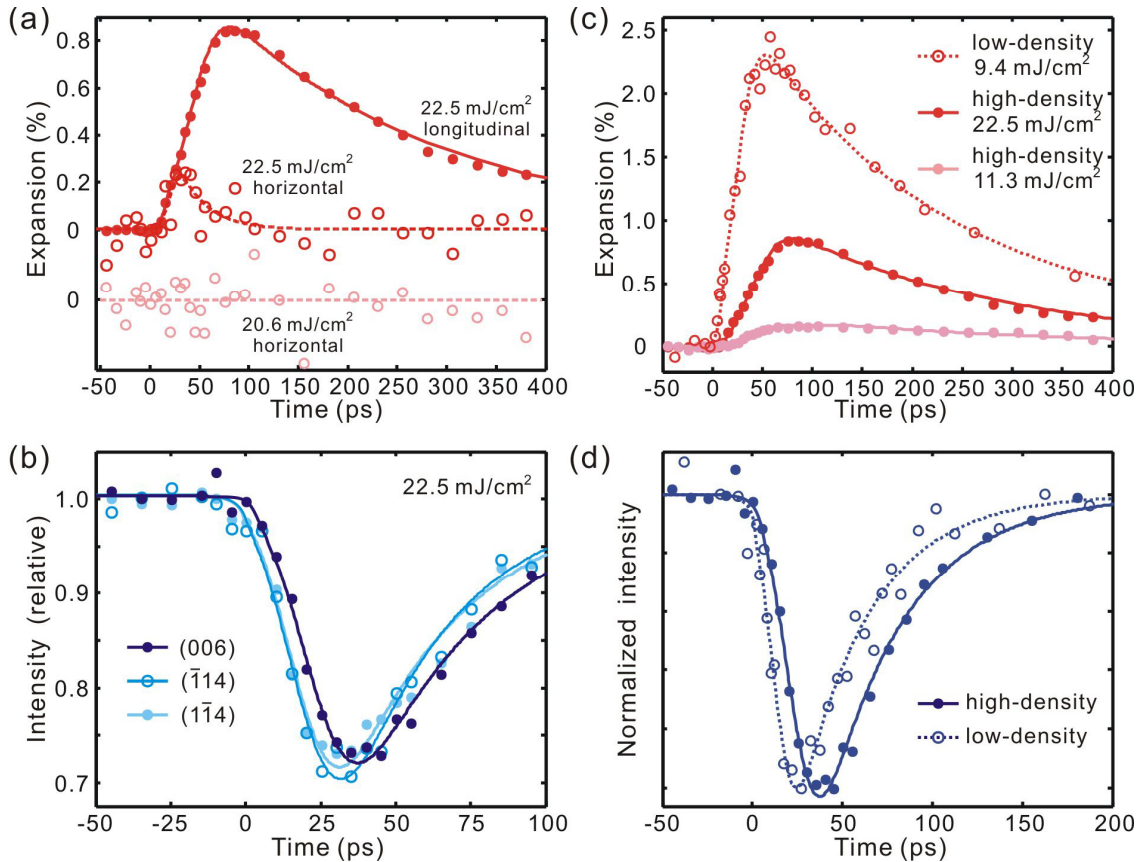


Fig. 5. Anisotropic expansions and density effect. Comparison between the longitudinal and horizontal structural dynamics and between the longitudinal dynamics obtained for the high- and low-density arrays. (a) Horizontal expansion of a wire (open circles) obtained from the horizontal spacing between $(\bar{1}14)$ and $(1\bar{1}4)$ Bragg spots; it is much smaller when compared to the longitudinal expansion (dots), and is only seen at our highest fluence. It also exhibits a faster decay. (b) The intensities of $(\bar{1}14)$ and $(1\bar{1}4)$ spots decrease at earlier time than that of the (006); their temporal behaviors are alike, however. (c and d) Longitudinal expansion and diffraction intensity of the low-density array (open circles) share similar overall temporal evolution with those from the high-density array (dots), but rise on a faster time scale. Even at a smaller excitation fluence, the c -axis expansion of the wires in the low-density array is significantly larger than that obtained at higher fluences for the high-density array (c).

for different spots). Quantitative analysis was carried out by fitting the vertical and horizontal intensity profiles of Bragg spots with a pseudo-Voigt function, yielding temporal evolution profiles not only of the spot intensities and positions but also of the widths (Fig. 3b). Because of the high signal-to-noise ratio and the high order of diffraction, the c -axis expansion (deduced from the spot vertical position) can be determined with an accuracy of 0.007%; the diffraction intensity and peak width standard deviations are 0.75% and 1.2%, respectively (see the data in Figs. 4 and 5). The sensitivity of our UEC apparatus allows for detection of small diffraction changes as seen in Fig. 4, panels b to d, for the low fluence cases. Typical behavior is shown for the (006) spot: whereas the intensity and vertical width are very similar in behavior and nearly recover (Fig. 4a) in only 200 ps, the rise of expansion along the c -axis is delayed in time by ~ 15 ps and decays on a much longer time scale, reaching completion in about 1 ns.

The fluence dependence of the expansion, intensity and width indicates the role of the (electron-hole) carriers. When the maximum c -axis expansion is plotted as a function of fluence in a log–log plot, the dependence follows a linear relationship with a slope value of 2.5 (Fig. 4b, inset). The energy of the excitation photon is less than half of the energy gap of ZnO (3.37 eV) (10, 18), and also less than half of the energy gap of wurtzite GaN (3.44 eV) (11). Thus, the carriers are generated in the ZnO nanowires by energetically allowed three-photon excitation (3PA) and/or by enhanced two-photon absorption (2PA), both of which are due to the geometry of the nanostructure. We failed to observe diffraction changes when the experiments were repeated on a single-crystal ZnO sample (0.5 mm thick) at the highest fluence, suggesting a significant change in the band gap/carrier density in the wires.

Based on the band structure of ZnO (18), the excitation by 2PA generates carriers

of somewhat lower energy than the band gap in the Γ region where the momentum is zero; by 3PA, the above-gap excitation becomes possible in the Γ –M(K) regions with momentum along $\langle 110 \rangle$ ($\langle 100 \rangle$). We found consistent studies in the literature. It has been reported that for ZnO crystals, the 2PA is negligible; the 3PA is weak, with a coefficient of $\sim 0.01 \text{ cm}^3/\text{GW}^2$ and saturation intensity of tens of GW/cm^2 at 800 nm (22, 23). The vertically aligned ZnO wires exhibit significant enhancement of optical nonlinearities: the 2PA coefficient (α_2) is greater than $10^3 \text{ cm}/\text{GW}$ (24, 25) and the wires show strong 3PA at high excitation intensities (26). The increased multiphoton absorption has been attributed to the local-field enhancement due to the surface states and the interaction between the aligned wire facets (24). Using the 2PA coefficient of $\alpha_2 \sim 4 \times 10^3 \text{ cm}/\text{GW}$ the effective penetration depth at an intensity of $I = 75 \text{ GW}/\text{cm}^2$ is $\sim 33 \text{ nm}$. However, because of saturation, this length can reach micrometers, which results in a more uniform excitation of the wires.

The change of the expansion, intensity and width at different fluences rises after the zero of time and reaches the maximum value nearly at the same time, also consistent with the fact that the wires were directly excited and not heated through a substrate with energy transport through the wire. The temporal evolution profiles of the lattice expansion, intensity and width can be fitted with the following formula, $M(t)$, convoluted with our instrumental Gaussian response function (27),

$$M(t) = A \cdot \left[\exp\left(-\frac{t}{\tau_{decay}}\right) - \exp\left(-\frac{t}{\tau_{rise}}\right) \right] + A(0) \quad \text{for } t > 0,$$

$$= A(0) \quad \text{for } t < 0$$

where A and $A(0)$ are the amplitudes from the induced structural change and at negative times, respectively, and τ_{rise} and τ_{decay} are the time constants for the rise and decay parts

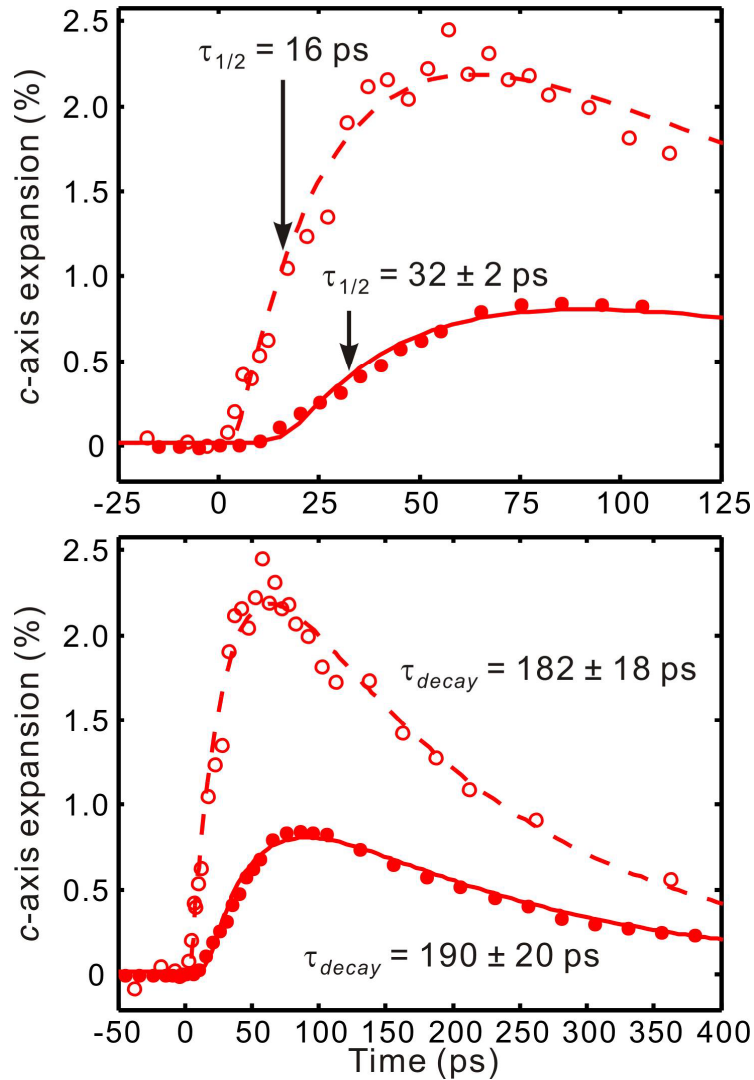


Fig. 6. Temporal evolution of the longitudinal expansion at short-time (upper panel) and long-time (lower panel) scales (Fig. 5c). Both the low-density (open circles and dashed line) and high-density (solid dots and line) nanowire arrays are displayed. The overall dynamics are similar, but the low-density array exhibits a faster rise [τ_{rise} (low density) = $26 \pm 3 \text{ ps}$] and larger amplitude in comparison with those of the high-density array [τ_{rise} (high density) = $36 \pm 6 \text{ ps}$]. The error bars given in the figure are the step size in the experiments for experimentally determined $\tau_{1/2}$ (upper panel) and standard deviations from the fits (lower panel); because the rises are relatively slow (on the picosecond time scale), there was no need to record the entire profiles with femtosecond steps.

of the change, respectively. For time-resolved electron diffraction of condensed matter, however, the response function accounts for the diffraction *difference* following the optical excitation, since electrons can probe all structures. All solid lines in Fig. 4 and all lines in Fig. 5 were obtained by such fitting (see Fig. 6 for the results of fitting for Fig. 5c as an example). Without losing the physical significance, we shall use the experimentally determined times at half maximum $\tau_{1/2}$ for further discussions.

In Fig. 4a, $\tau_{1/2} = 17$ ps for the intensity and width, and $\tau_{1/2} = 32$ ps for the expansion. The in-plane component of the nanowire, i.e., the horizontal lattice expansion derived from the change in the horizontal spacing between $(\bar{1}14)$ and $(1\bar{1}4)$ spots, is much smaller and only noticeable at the highest fluence, with a significantly faster recovery time (Fig. 5a). The intensity change of $(\bar{1}14)$ and $(1\bar{1}4)$ spots share a similar temporal evolution with that of the (006) spot, but are shifted to earlier time by ~ 5 ps (Fig. 5b). Lastly, as noted in Fig. 5c, the c -axis expansion is higher in amplitude for the low-density array and rises faster than the rate observed for the high-density array.

From the results presented for structure, dynamics and fluence and density dependences, the following picture emerges. The wires display correlated, nonequilibrium behavior in that the behavior is anisotropically driven by the potential of the carriers generated by the excitation, i.e., by the electronic change in bonding. Thermal expansion of the material [using the coefficient $\alpha_c = 2.49 \times 10^{-6} \text{ K}^{-1}$ (18)] would give $\Delta c/c \sim 2 \times 10^{-4}$ ($\Delta T \sim 80$ K), which is two orders of magnitude smaller than the observed values. At the highest fluence used, the observed expansion of 1~2% would correspond to a temperature rise of 4000~8000 K, far beyond the decomposition temperature of 1975 K (18). In other words, the dynamics are not controlled by a thermal-like, incoherent expansion due to bonding anharmonicity but, instead, by the buildup of amplitudes due to

the collective motions of atoms in the wire.

In a one-dimensional model, which considers the influence of a force induced by the excitation field, we can calculate the diffraction resulting from wave-like atomic motions in the wires. The speed of sound along the c -axis in ZnO is 6200 m/s and, over the wire length (2 μm), a round-trip wave recurrence of 650 ps would be expected, if the force field is impulsive (see Fig. 2b of Ch. 12), contrary to what was observed. Instead, we observed a buildup of expansion and gradual recovery on a longer time scale (Fig. 4b), a behavior which is obtainable when a sustaining excitation force field is operative (see Fig. 4a of Ch. 12). This sustaining force is the result of carriers' persistence and the potential they generate over the excitation length, on the micrometer scale in this case.

The anisotropic expansion reflects an induced antibonding character along the wire direction. Since the initial carrier generation is near Γ (by 2PA) and in the in-plane Γ -M(K) region (by 3PA), carrier-carrier scattering becomes necessary in order to reach the Γ -A region along the wire, z direction (the Zn-O bonding). We also note that the promptness of the intensity and width change comes from the direct cascade of optical (and acoustic) phonon generation, which in this case amounts to ~ 20 for 3PA. As a result, the maximum vertical expansion lags in time the change of both the intensity and width. Besides the temporal behavior discussed, several observations support this conclusion. First, the restructuring for the expansion occurs on a much longer time scale than those of the intensity and width, and it is similar to the decay time of photoluminescence (radiative recombination) of ~ 1 to 2 ns (28). Second, the horizontal expansion is absent at lower fluences, and appears and disappears on a much shorter time scale at our highest fluence (Fig. 5a). This is because the initial excitation induces in-plane movements of atoms, which also signifies that the intensity of $(\bar{1}14)$ and $(1\bar{1}4)$ spots should

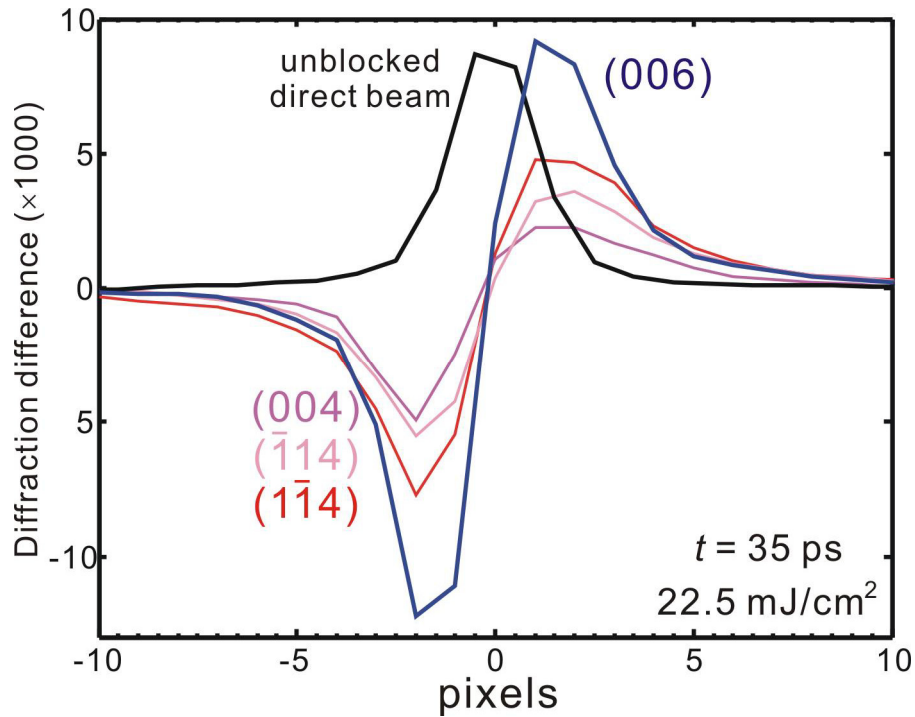


Fig. 7. Diffraction difference for several Bragg spots along the vertical direction (Fig. 3a).

decrease before that of the (006), as observed experimentally. Lastly, as the excitation fluence increases, the density of carriers increases, leading to the observed larger longitudinal expansion.

When these different sets of experiments were repeated on the low-density nanowire array (Fig. 5, panels c and d), we observed similar behavior to that of the high-density array, but with the largest expansion reaching as much as 2% and occurring at earlier times. These observations suggest that in the low-density materials, the nanowires are freer to collectively expand, reaching a nonequilibrium effective “temperature” of 8000 K through the electronic potential change (Zn–O bond weakening) by carriers. Modeling of the electronic–nuclear coupling may quantify this behavior. Although the average separation between wires is 300 nm in the high-density array, the inhomogeneity in distribution (clustering) becomes essential to the extent of expansion.

The Issue of Similar Movement for Different Spots

We have noticed the similar amount of movement for different Bragg spots (Fig. 7), and the allegation of an overall pattern shift due to certain charge effects might seem legitimate. It should be noted that our discovery of a unidirectional behavior in ZnO nanowires, induced by an ultrashort infrared light pulse and probed by electrons, was concluded not only from the movement of few Bragg spots but also from the temporal intensity and width changes in the diffraction. Each of the diffraction features as a function of time has its direct association with certain atomic or lattice motions in the structure, and their response differences in time mirror the processes that occur subsequently in a material. Given the resembling but different temporal dependence for the diffraction features (Fig. 4a), there should be more than one physical process involved in the dynamics of a zinc oxide nanowire. In addition, as mentioned earlier, the lack of a movement over time for the unblocked (undiffracted) direct beam undoubtedly eliminates the explanation of a simple overall pattern shift for our observation.

Photoemission from ZnO wires could not lead to our experimental findings, either. The work function of ZnO is ~ 5 eV (29, 30), larger than the energy provided by three photons of 800-nm light. Besides, such a charge separation would result in a positive potential on the material surface and affect the trajectory of the undiffracted grazing electrons, which is in contradiction to our finding. Furthermore, the diffraction intensity and width changes over time would become inexplicable should the single mechanism of photoemission be responsible. On the contrary, the physical processes mentioned above satisfactorily explained our experimental results; e.g., the fluence dependence of *c*-axis expansion in a log–log plot correctly matches with our proposed model of multiphoton excitation. In fact, the fluence dependence of maximum intensity decrease in a log–log

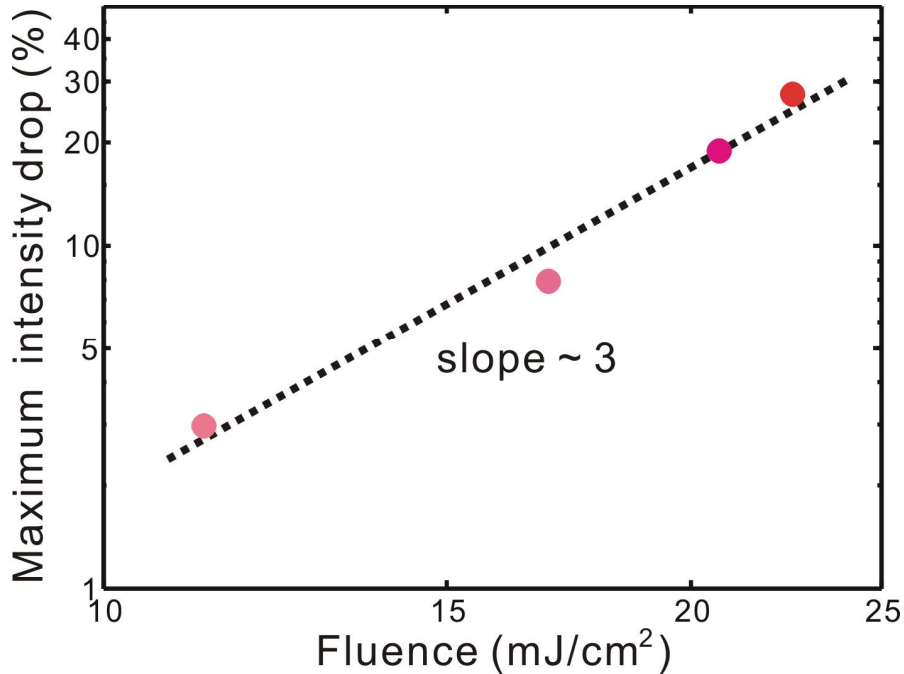


Fig. 8. The fitted slope in the log-log plot indicates that the maximum intensity decrease is proportional to the fluence to the power of 3. (Fig. 4c).

plot has a slope of ~ 3 (Fig. 8), which is again in a nice agreement with the required 3-photon absorption.

It should also be noted that proportionality of the vertical movement versus the order of the diffraction spot (in accordance with $\Delta c/c = -\Delta s_{\perp}/s_{\perp}$) would be valid only if all the spots were from the same structure. Whereas the (006) spot and first-order-Laue-zone diffractions were generated from the reflection nature of our technique, the appearance of other spots, such as (004), $(1\bar{1}4)$ and $(\bar{1}14)$, was due to the transmission-type probing of the current nanostructure. Given the proximity of these spots to the shadow edge, the responsible diffracting structure was only the top of the nanowires where the lattice is free to expand; electron transmission from a lower part could be easily blocked by other adjacent wires. The (006) spot, however, had contribution from both the top and a lower part of tens of nanometers, leading to an averaged, slightly lowered, c -axis expansion. A

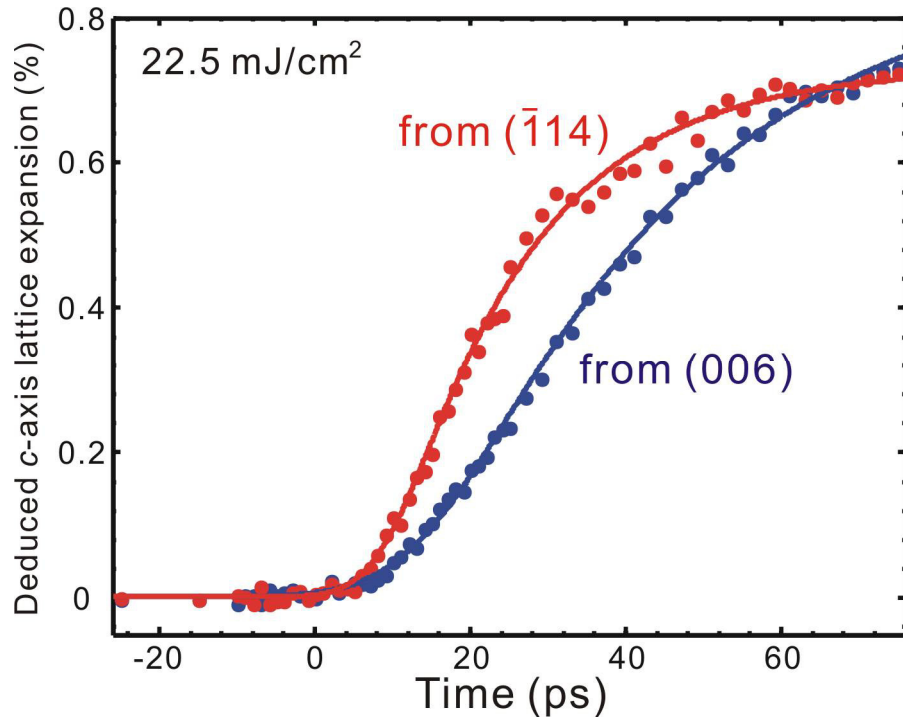


Fig. 9. Longitudinal lattice expansion deduced from the vertical movement of the $(\bar{1}\bar{1}4)$ and (006) spots. The different speed for the rise signifies that the diffractions do not originate from exactly the same part of a nanowire.

natural consequence of this explanation will be an earlier start of spot shift for the (004), $(1\bar{1}4)$ and $(\bar{1}\bar{1}4)$ diffractions, and indeed our analysis supports such a model (Fig. 9).

Conclusion

Visualization of atomic motions during structural change reveals the direct role of electron–nuclear correlations which ultimately control the behavior of macroscopic phenomena, such as the optoelectronic effect in zinc oxide. The unexpected material behavior described above for confined nanostructures is unobservable when the studies are made in the equilibrium state. Only when observed with atomic-scale spatial and femtosecond temporal resolutions can we acquire fundamental understanding of structural perturbations and relaxations for different optical and chemical dopings, and

hence the optimization of function at the nanometer scale.

References:

1. M. L. Steigerwald, L. E. Brus, *Acc. Chem. Res.* **23**, 183 (1990).
2. S. Iijima, *Nature* **354**, 56 (1991).
3. G. M. Whitesides, J. P. Mathias, C. T. Seto, *Science* **254**, 1312 (1991).
4. Y. Cui, Q. Wei, H. Park, C. M. Lieber, *Science* **293**, 1289 (2001).
5. A. P. Alivisatos, *Science* **271**, 933 (1996).
6. C. B. Murray, C. R. Kagan, M. G. Bawendi, *Ann. Rev. Mater. Sci.* **30**, 545 (2000).
7. Y. Xia *et al.*, *Adv. Mater.* **15**, 353 (2003).
8. Z. L. Wang, *J. Phys.: Condens. Matter* **16**, R829 (2004).
9. Z. L. Wang, *Mater. Today* **10**, 20 (2007).
10. Ü. Özgür *et al.*, *J. Appl. Phys.* **98**, 041301 (2005).
11. X. Wang *et al.*, *J. Am. Chem. Soc.* **127**, 7920 (2005).
12. L. E. Greene *et al.*, *Nano Lett.* **5**, 1231 (2005).
13. P. Baum, A. H. Zewail, *Proc. Natl. Acad. Sci. USA* **103**, 16105 (2006).
14. N. Gedik, D.-S. Yang, G. Logvenov, I. Bozovic, A. H. Zewail, *Science* **316**, 425 (2007).
15. P. Baum, D.-S. Yang, A. H. Zewail, *Science* **318**, 788 (2007).
16. F. Carbone, P. Baum, P. Rudolf, A. H. Zewail, *Phys. Rev. Lett* **100**, 035501 (2008).
17. Z. L. Wang, *Reflection electron microscopy and spectroscopy for surface science* (Cambridge Univ. Press, Cambridge, 1996).
18. S. Adachi, Ed., *Handbook on Physical Properties of Semiconductors*, vol. 3 (Kluwer Academic Publishers, Boston, 2004).

19. A. Ichimiya, P. I. Cohen, *Reflection High Energy Electron Diffraction* (Cambridge Univ. Press, Cambridge, 2004), pp. 20-23.
20. B. E. Warren, *X-ray diffraction* (Dover, New York, 1990).
21. E. Müller *et al.*, in *Microscopy of Semiconducting Materials* (Springer, New York, 2006), pp. 303-306.
22. J. He, Y. Qu, H. Li, J. Mi, W. Ji, *Opt. Express* **13**, 9235 (2005).
23. B. Gu, J. He, W. Ji, H.-T. Wang, *J. Appl. Phys.* **103**, 073105 (2008).
24. H. W. Lee *et al.*, *Chem. Phys. Lett.* **447**, 86 (2007).
25. S. Xiao *et al.*, *Chin. Phys. B* **17**, 1291 (2008).
26. C. F. Zhang, Z. W. Dong, G. J. You, S. X. Qian, H. Deng, *Opt. Lett.* **31**, 3345 (2006).
27. S. Pedersen, A. H. Zewail, *Mol. Phys.* **89**, 1455 (1996).
28. M. H. Huang *et al.*, *Science* **292**, 1897 (2001).
29. K. Jacobi, G. Zwicker, A. Gutmann, *Surf. Sci.* **141**, 109 (1984).
30. X. Bai, E. G. Wang, P. Gao, Z. L. Wang, *Nano Lett.* **3**, 1147 (2003).